

Rapid Laurentide Ice Sheet growth preceding the Last Glacial Maximum due to summer snowfall

Received: 15 September 2022

Accepted: 12 March 2024

Published online: 12 April 2024

 Check for updates

Lu Niu  , Gregor Knorr , Uta Krebs-Kanzow, Paul Gierz  & Gerrit Lohmann 

There has been extensive research into the nonlinear responses of the Earth system to astronomical forcing during the last glacial cycle. However, the speed and spatial geometry of ice sheet expansion to its largest extent at the Last Glacial Maximum 21 thousand years ago remains uncertain. Here we use an Earth system model with interactive ice sheets to show that distinct initial North American (Laurentide) ice sheets at 38 thousand years ago converge towards a configuration consistent with the Last Glacial Maximum due to feedbacks between atmospheric circulation and ice sheet geometry. Notably, ice advance speed and spatial pattern in our model are controlled by the amount of summer snowfall, which is dependent on moisture transport pathways from the North Atlantic warm pool linked to ice sheet geometry. The consequence of increased summer snowfall on the surface mass balance of the ice sheet is not only the direct increase in accumulation but the indirect reduction in melt through the snow/ice–albedo feedback. These feedbacks provide an effective mechanism for ice growth for a range of initial ice sheet states and may explain the rapid North American ice volume increase during the last ice age and potentially driving growth during previous glacial periods.

Marine Isotope Stage 3 (MIS 3, about 60–29 thousand years ago (ka)) was a relative warm period during which the glaciation process was roughly halfway towards the Last Glacial Maximum (LGM, -21 ka) within the last glacial cycle^{1,2}. In parallel, millennial-scale abrupt climate shifts (known as Dansgaard–Oeschger oscillations) occurred more frequently before 32 ka than thereafter³. The final glaciation from MIS 3 to the LGM starting after -38 ka was also characterized by a gradual decrease in boreal summer insolation^{4,5}, decreasing greenhouse gas (GHG) concentrations (for example, refs. 6–8) in the atmosphere (Fig. 1a), advancing Northern Hemisphere ice sheets and a sea-level drop in the order of tens of metres (for example, refs. 9–13) (Fig. 1h, dots/dotted lines).

However, large uncertainties in ice sheet configurations and associated ice growth persist from MIS 3 to the LGM, given that the glacial geomorphological record from this period is mostly erased by the

following ice sheet expansions^{2,14–18}. Consequently, both ice sheet and sea-level reconstructions during MIS 3 show a considerable diversity, with differences in estimations of global mean sea level up to 60 m (refs. 13,18–21). Particularly, recent work proposed that the Laurentide Ice Sheet (LIS) volume could be substantially reduced (for example, ref. 20). Interestingly, despite the large spread in ice sheet/sea-level reconstructions during MIS 3 using different reconstruction methods, monotonically rapid decreases in sea level after around 32 ka are consistently depicted across these reconstructions (Fig. 1h)²². Moreover, given such fundamental ice sheet differences before the final phase of ice growth it is open to question how these differences impact on the North American ice sheet evolution towards the LGM.

So far, investigations with complex Earth system models focusing on this period are relatively sparse. Moreover, the underlying climate

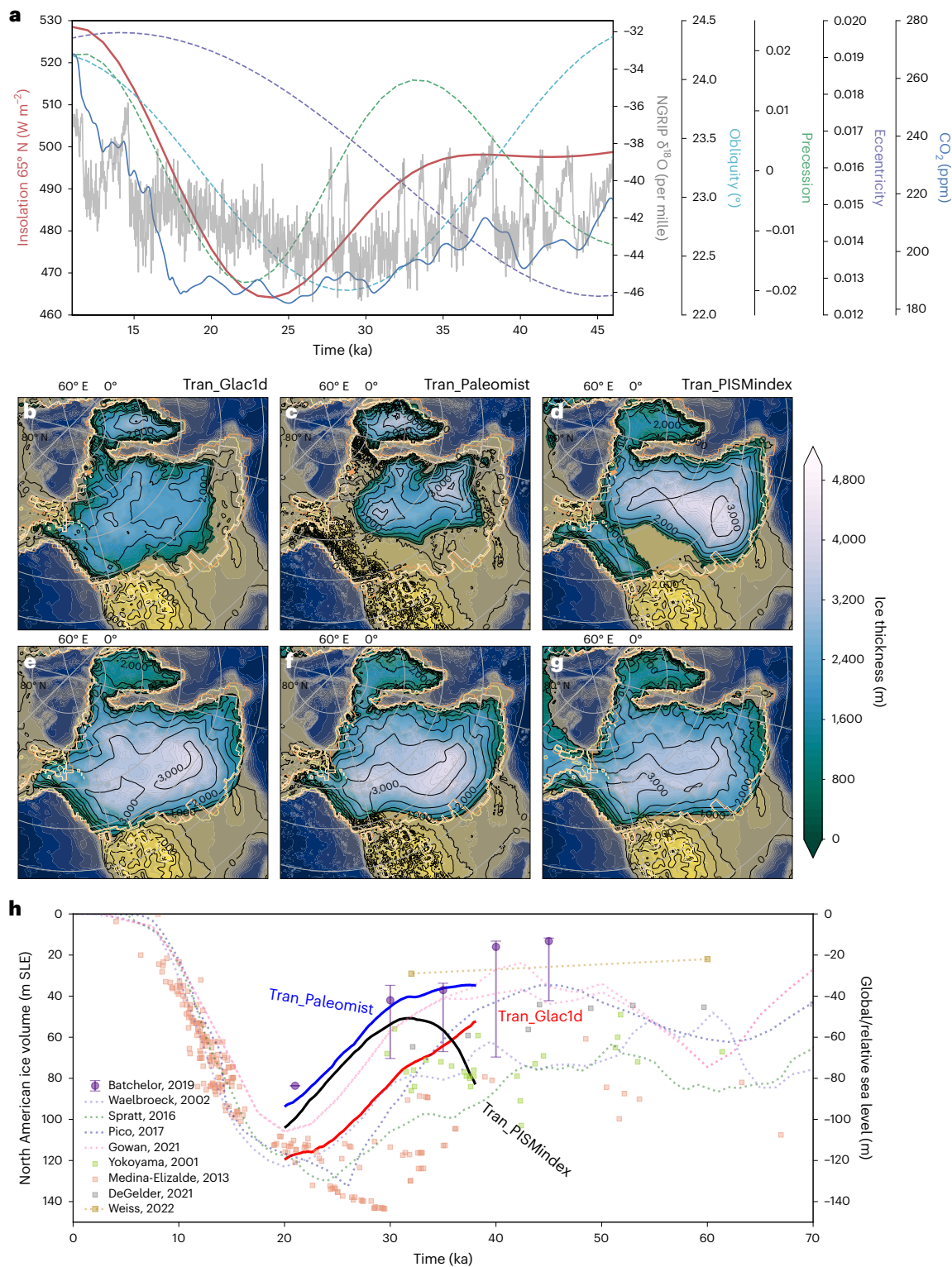


Fig. 1 | Boundary conditions, such as orbital parameters, CO₂ values and North American ice sheet initial configurations, and spatial and temporal patterns of the simulated ice sheets. a, Insolation at 65° N at June solstice (red), CO₂ (dark blue), obliquity (light blue), precession parameters (green), eccentricity (purple) and Greenland ice core records (grey)^{3,5,8}. **b–d**, Reconstructed ice thickness at 38 ka from Glac1D¹⁹ (**b**), Paleomist¹³ (**c**) and a glacial index simulation using PISM standalone model (PISM-index) (**d**). Black contours depict surface elevation with a 500-m interval. Yellowish contours denote reconstructed ice sheet extents from different reconstruction datasets (Glac1D, Paleomist and Ice6g⁵³) at 21 ka. Grey lines and circles show longitude

and latitude, respectively. The basemaps are drawn using the reconstruction datasets. **e–g**, Corresponding simulated ice thickness distributions (ice volume of -100 m in sea-level equivalent, m SLE) for experiments Tran_Glac1d (**e**), Tran_Paleomist (**f**) and Tran_PISMindex (**g**). **h**, Evolution of ice volume of the North American ice sheets from different experiments (solid lines), in comparison with ice volume estimations based on reconstructed North American ice margins⁵⁴ (Methods, purple solid circles represent the best estimates, error bars indicate the maximum and minimum estimates) and reconstructed global/relative sea-level data^{11,13,18,55–59} (Methods). The time axis corresponds to the ice sheet model years.

conditions and ice sheet evolution are often examined separately due to computational constraints: climates at certain time slices are simulated using comprehensive General Circulation Models (GCMs) with fixed ice sheet boundaries, whereas ice sheet simulations use climates derived from the GCM output. This leads to mis-/inadequate representations of internal feedbacks between ice sheets and other Earth system components (such as ice–albedo feedback and readjustments of atmospheric circulation), yet their impact could be important²³. Although transient simulations on glacial–interglacial timescales could also be conducted with Earth system models of intermediate complexity, for example, refs. 24,25, these models typically have relatively coarse spatial resolutions, and representations of more advanced atmospheric–ocean dynamics are limited.

Therefore in this study, we aim at a complex modelling approach allowing for a comprehensive representation of internal climate feedbacks, using a comprehensive state-of-the-art Earth system model with interactive ice sheets (AWI-ESM). Our study aims to disentangle the physical processes that are responsible for the ice sheet growth from an intermediate size towards the LGM with a focus on coupled atmosphere–ocean–ice sheet interactions. Due to the computational burden of our comprehensive coupled model approach, we use an asynchronous coupling scheme in our study (Methods). Note that neither the resemblance of a specific trajectory of ice volume changes nor the simulation of the exact timing of the LGM conditions are the aim of this study. In our comprehensive coupled climate–ice sheet model simulations, we reproduce the fast growth of the ice sheet from MIS 3 to the LGM. One of the key processes in this ice sheet expansion involves adjustments in moisture transport from the low latitudes of the Atlantic basin and summer snowfall. This causes a convergence towards a LGM ice sheet configuration, regardless of the choice of the initial state of the MIS 3 ice sheet.

Convergent LIS evolution

At first, three transient simulations (experiments Tran_Glac1d, Tran_Paleomist and Tran_PISMindex) are conducted with the same insolation⁵ and GHG⁸ changes covering the period from 38 ka to 20 ka (Fig. 1a). These experiments only differ in their initial ice sheet configurations (especially over North America) at the starting point 38 ka as they are based on three different ice sheet reconstructions (Glac1D-38k, Paleomist-38k and PISM-index-38k; Fig. 1b–d). Two of the initial conditions are taken from the glacial isostatic adjustment (GIA)-based ice sheet reconstructions Glac1D¹⁹ and Paleomist³, respectively. Another initial condition is obtained by a standalone ice sheet simulation using a glacial index method (PISM-index, Methods). The ice coverage in Glac1D-38k is comparatively extensive (the southwestern margin of the LIS almost reaches the LGM extent), whereas in Paleomist-38k ice sheets are considerably reduced. In PISM-index-38k, an asymmetrical distribution of the LIS is exhibited, with the ice sheet over the eastern region being more extensive, while largely reduced over the western region.

Starting with our experiments at 38 ka, a high boreal summer insolation until ~32 ka prevents a pronounced ice sheet growth of the LIS and Cordilleran ice sheet (CIS) (Fig. 1h and Extended Data Fig. 1a–c). The increases of ice volume start to speed up as the insolation continues to decrease. For experiments initialized from the Glac1D-38k boundaries, the LIS first shows a pronounced eastward advance before expanding southward. For experiments with Paleomist-38k initial condition, the LIS continues to expand in multiple directions (east, west and south). For experiments with PISM-index-38k as a starting condition, substantial ice sheet advance occurs in the discontinuity between the LIS and CIS, although ice retreats in the eastern area in response to high insolation before 32 ka. In the end, the simulated LIS evolves into configurations that match with the reconstructed LGM extents (Fig. 1e–g).

To eliminate the effects of transient insolation and GHG changes in a quasi-equilibrium perspective, similar experiments but with fixed

21 ka insolation and GHGs are conducted (experiments 21k_Glac1d, 21k_Paleomist and 21k_PISMindex). As a result of comparatively low insolation, the glacial advances of the ice sheets are faster (compared individually to their transient counterparts), but the spatial extents of the ice sheets are rather similar (Extended Data Fig. 1d–f). The simulated ice sheets first advance to LGM-like configurations and then further advance to a quasi-equilibrated configuration (Extended Data Fig. 2).

Although large initial differences are visible among Glac1D-38k, Paleomist-38k and PISM-index-38k ice sheets, all of the simulated ice sheets evolve into states that show a reasonable match with the reconstructed LGM extents. It indicates that internal climate feedbacks between ice sheets and other climate components play an important role, as they lead to readjustment of the mass balance of the ice sheets.

Spatial heterogeneities in surface mass balance changes

To understand the convergent evolution of the North American ice sheets, the spatial distributions of the surface mass balance (SMB) for ice sheets at intermediate sizes (70 m SLE) both in summer and winter are compared (Fig. 2 and Extended Data Fig. 3). Distinct spatial patterns are shown in summer SMB (Fig. 2d–f), whereas winter SMB patterns hardly differ among experiments (Extended Data Fig. 3a–c). Consistent with the positive SMB patterns, snowfall is more intense in summer across all experiments, with the spatial patterns exhibiting greater differences than those shown in winter (Fig. 2g–i and Extended Data Fig. 3d–f). In general, the positive SMB/snowfall is enhanced in summer when the southern margin of the ice sheet deviates from a zonal orientation in different experiments, which seems to counteract the asymmetric distributions of the LIS.

To understand spatial heterogeneities in SMB through time, we present Hovmöller diagrams illustrating the annual mean SMB changes over the southern ice sheet margin (ice thickness of 0–2,500 m) through time at different longitudes (Fig. 3d–f, shaded) and changes in the latitudes of the southern ice sheet margin (Fig. 3d–f, contour lines). Besides at the east and west coasts, a particularly positive SMB centre is detected in the interior of the North American continent. Although the patterns vary among different experiments, this centre always exhibits a continuous westward migration over time and seems to be consistent with the rapid ice sheet expansions (Fig. 3d–f, contour lines). Large positive SMB is simulated where the southern margin of the ice sheet is in northwest to southeast orientation, which supports a gradual reduction in the asymmetry of the ice sheet distribution.

Moreover, we separate the SMB changes into summer (including accumulation and ablation zones) and winter contributions and we find that positive SMB centres are dominated by changes in summer (Fig. 3g–i and Extended Data Fig. 4a–f). The trajectory of maximal annual mean SMB centres is not only corresponding with an increase in positive SMB in the accumulation zone but also with a reduction in the intensity of negative SMB in the ablation zone. Overall, the most rapid expansion of the southern ice sheet is controlled by both increased accumulation and reduced ablation during summer, whereas no pronounced changes are detected during winter for the LIS.

The underlying processes and the role of summer snowfall

To determine the cause of the SMB changes, we compare the snow/precipitation and surface air temperature changes (Fig. 3m–o and Extended Data Figs. 4g–i and 5). For the LIS, snowfall variations in summer strongly resemble the total SMB variations, and the summer SMB changes over both the accumulation and ablation zones (Fig. 3d–l). In contrast, no obvious linkage is shown between the surface air temperature and the ice sheet expansion patterns (Extended Data Fig. 5).

To gain a deeper process understanding, the seasonal variations of SMB components along a certain longitude (97° W) through time are

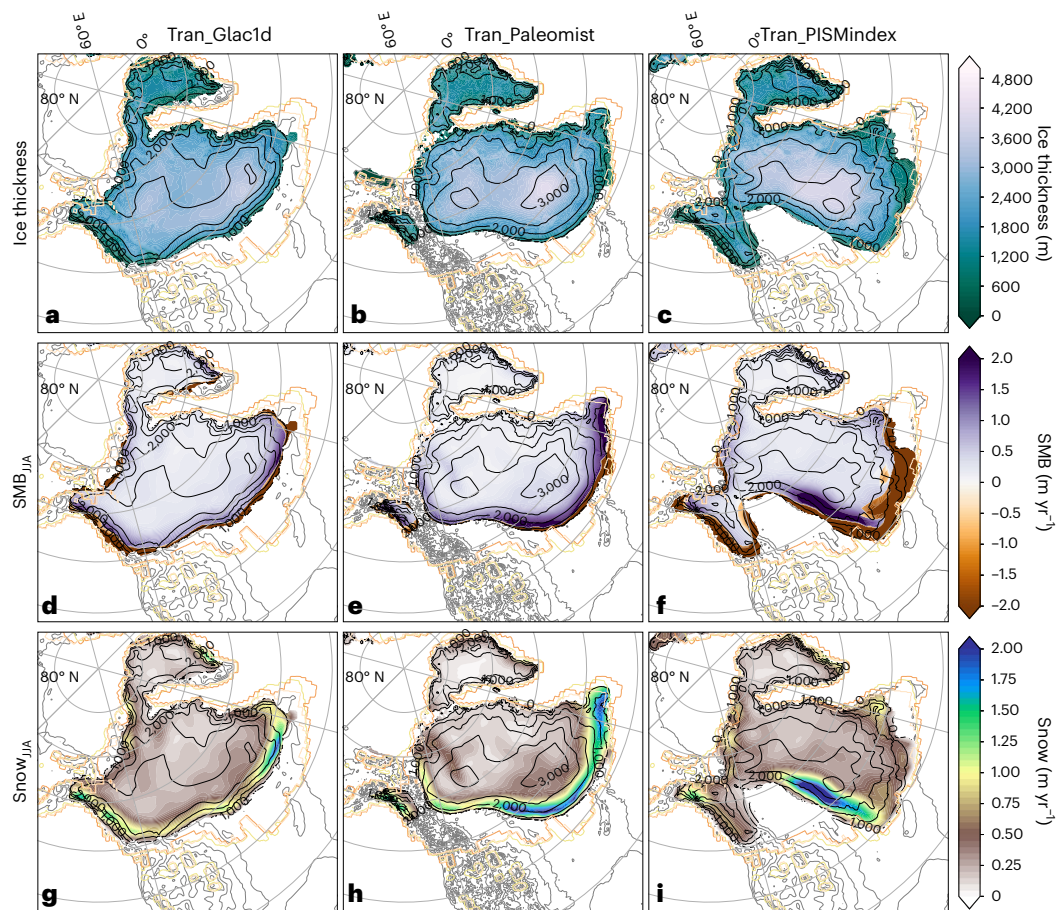


Fig. 2 | Simulated intermediate states of the North American ice sheets, the related surface mass balance and snowfall in summer. a–c, Ice thickness distributions of the North American ice sheets at intermediate sizes (70 m SLE) from different experiments: Tran_Glac1d (a), Tran_Paleomist (b), Tran_PISMindex (c). **d–f,** The corresponding SMB over ice sheets in summer (JJA). **g–i,** The

corresponding snowfall over ice sheets in summer (JJA). Black contours depict surface elevation with a 500-m interval. Yellowish contours are reconstructed ice sheet extents from different datasets (Glac1D, Paleomist and Ice6g) at 21 ka. Grey lines and circles indicate longitude and latitude, respectively.

quantitatively compared over areas with rapid ice expansions (Fig. 4). Two important phases are shown for the ice sheet growth: From 32 ka, declining background temperatures reduce melt, and the annual mean SMB shifts from negative to near zero (Fig. 4a,c,e). Thereafter (after ~28 ka), precipitation/snowfall largely increases over the south of the LIS southern margin, whereas the near-surface temperature shifts from a decreasing to an increasing trend as ice sheet advances towards lower latitudes (Fig. 4a,d). For LIS, more snowfall accumulates from May to October than from November to April (snowfall during summer is roughly twice as large as that during winter; Fig. 4e). Corresponding with periods of fast ice expansions (Fig. 4d), large positive total SMB is evident (Fig. 4e, red line). The increase in total SMB is not solely attributed to the large increase in accumulation (blue bars), it is also attributed to strong decrease in summer melt (orange bars). More interestingly, changes in melt are closely correlated with albedo variations in summer (Fig. 4f,g), whereas contributions linked to surface air temperature are less obvious because different temperatures can co-exist for the same albedo values, especially for relatively low values (Fig. 4g).

This points to snowfall as a key to variations in albedo, as intensified snowfall can strongly suppress the melt–albedo feedback (melt lowers albedo, which in turn enhances melt). To deduce the effect of summer snowfall, we conduct a sensitivity test (ST) on the SMB: we reduce the summer (JJA) snowfall to the respective winter (DJF) amount, while all other variables are kept unchanged, and recalculate the SMB over time (Fig. 4e, grey lines). In this ST, we find both a reduction in accumulation (grey dashed line) and an increase in melt

(grey dotted line), which is accompanied by a lowered summer albedo (Fig. 4f, grey line), resulting in a largely decreased total SMB (Fig. 4e, grey solid line). In this sense the underlying SMB dynamics can be interpreted as a direct (accumulation) and indirect (melt) effect of boosted summer snowfall, which reduces initial ice sheet asymmetries. These effects are also robust if insolation is kept constant after 30 ka (Fig. 4e,f, black line; experiment ST1, Methods), highlighting the importance of internal dynamics towards the establishment of full LGM ice sheet conditions.

Moisture transport pathways and a self-adaptive mechanism

Figure 5 illustrates the vertically integrated water vapour transport (arrows) and vertically integrated moisture flux convergence (VIMFC, shaded) at different ice sheet conditions. For the LIS, the water vapour sources seem to be related to different pressure systems in different seasons. In boreal winter, the LIS is influenced by southward shifts of the mid-latitude jet stream and the storm track system (Fig. 5d–f). However in summer, warm and humid low-level southerly winds are formed due to the northward shift of the Azores High (Fig. 5a–c). This pathway provides an effective atmospheric moisture bridge towards the interior of the continent. More specifically the water vapour stems from the Gulf of Mexico area in the relatively warm subtropics and is advected further north over the Great Plains before it reaches the southern margin of the LIS. Depending on the shape of the southern ice sheet margin, the wind pattern and the related precipitation centre are

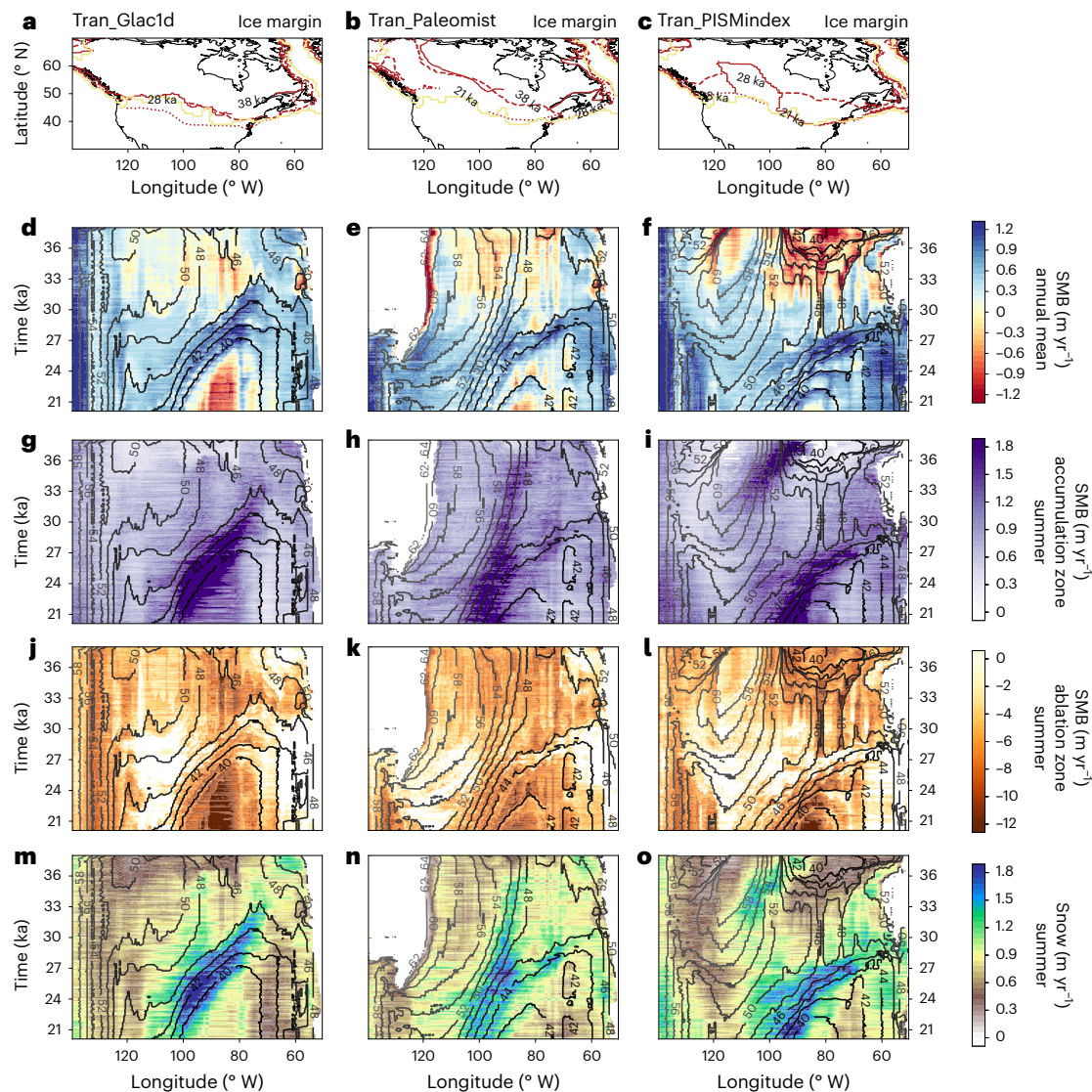


Fig. 3 | Annual mean and summer surface mass balance and summer snowfall changes of the North American ice sheets at different longitudes over time. a–c, Ice sheet margins at 38 ka, 28 ka and 21 ka from experiment Tran_Glac1d (a), Tran_Paleomist (b), Tran_PISMindex (c). **d–f,** Hovmöller Diagram of meridional mean total annual mean SMB of the North American ice sheets (NAIS) through different model years for experiment Tran_Glac1d (d), Tran_Paleomist (e), Tran_PISMindex (f). **g–i,** Same as **d–f**, but for summer (JJA) over the accumulation

zone. **j–l,** Similar as **g–i**, but over the ablation zone. **m–o,** Same as **g–i**, but for summer (JJA) snowfall. Black/grey contours in **d–o** are latitudes of the southern margin of the NAIS at different longitudes. The calculated areas are chosen with ice thickness between 0 m and 2,500 m. Contours that are dense along time axis indicate fast south expansion of the NAIS; contours that are dense along longitudes indicate longitudinally asymmetric distribution of the LIS. The time axis corresponds to the ice sheet model years.

also different. The strong enhancements of precipitation are favourable for LIS build-up. Water vapour from the west (Pacific) also partly influences the eastern LIS, but the strength is much smaller than from the south. For the CIS, water vapour is mainly transported from the Pacific Ocean (with more precipitation/snowfall simulated over the western coast during winter). This indicates that the CIS and LIS are possibly controlled by different atmospheric transport pathways.

On the basis of our results, we propose a self-adaptive mechanism of the LIS evolution (Fig. 6). The northward moisture transport in summer that controls the southern advancement of the LIS can in turn be redirected by the shape of the southern ice sheet margin. First, if the initial distribution of the LIS is Glac1D-38k-like (symmetric case in Fig. 6), more precipitation is over the southeastern margin (than the mid-western) which favours for the southeast expansion of the LIS. The presence of the Rocky Mountains could yield a warm and dry summer climate in the North American interior, which inhibits the western

expansion of the LIS during its build-up²⁶ (that is, towards a zonally asymmetric distribution). Secondly, if the ice sheet distribution is characterized by a more asymmetric configuration, the northward moisture transport pathway is re-arranged by the corresponding ice sheet orography. Consequently, more water vapour is transported farther north into the continental interior, which reduces the asymmetry of the ice sheet.

Implications for ice sheet evolution

In this study, we investigated the period of ice sheet growth from an intermediate size towards the LGM, using the state-of-the-art Earth system model AWI-ESM with interactive ice sheets. Our study emphasizes the important role of the internal climate feedbacks, especially the interplay between the atmospheric circulation and the ice sheet orography changes, on the ice sheet evolution. In particular for the final build-up of the LIS leading to the LGM, abundant moisture

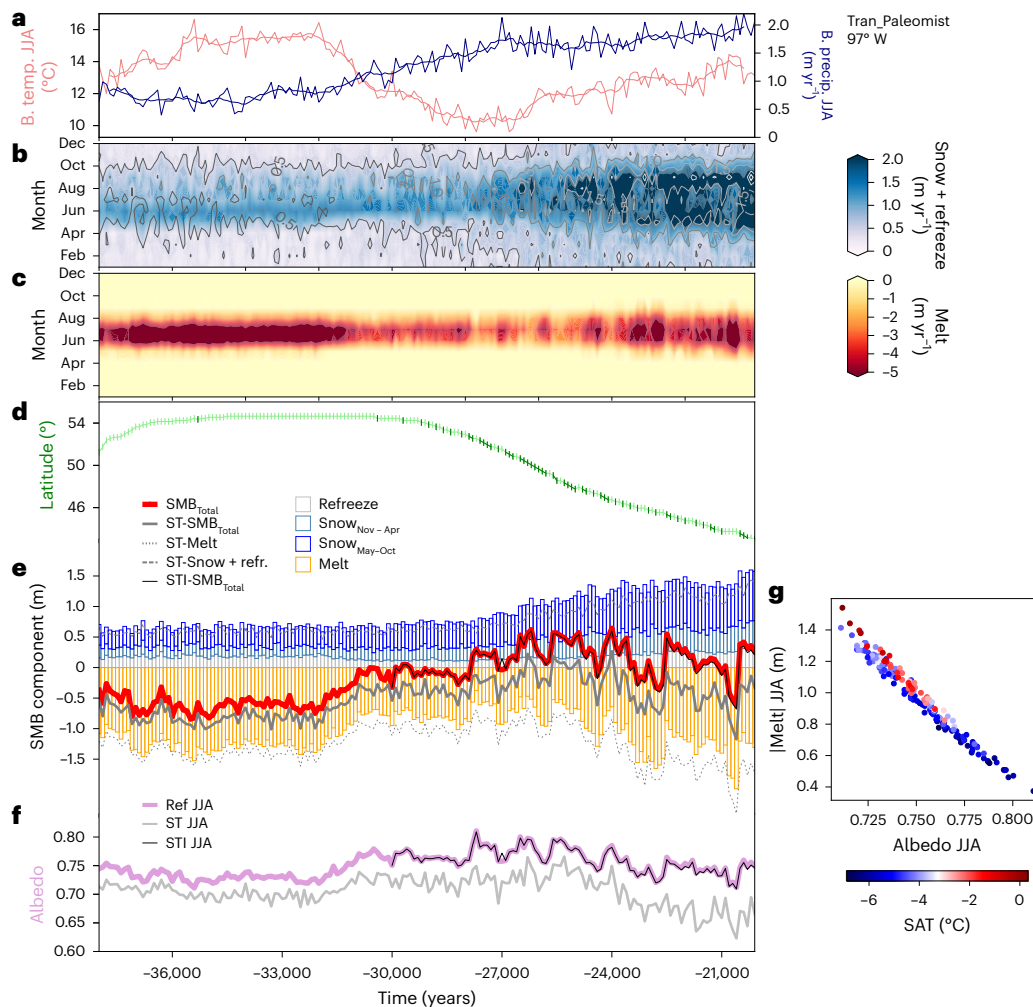


Fig. 4 | Monthly variations of SMB and snowfall, related changes of SMB components and background climate conditions along longitude 97° W through time in experiment Tran_Paleomist. **a**, Background temperature (B. temp.) and precipitation (B. precip.) variations in the south of the LIS southern margin at longitude 97° W in experiment Tran_Paleomist. **b**, Monthly variations of mean accumulation (including snowfall and refreeze, shaded) and snowfall changes (contour lines) over the southern LIS margin (with ice thickness from 0 to 2,500 m) along the same longitude. **c**, Same as **b** but for melt. **d**, Changes in latitudes of the LIS southern margin (green, with dark green indicating periods of southern advances). **e**, Changes in SMB components: total annual SMB (red line),

refreeze (refr., grey bars), snowfall of winter half year (November to April, light blue bars), snowfall of summer half year (May to October, dark blue bars), melt (orange bars). And variations of related SMB components from sensitivity test experiments (Methods) with reduced summer precipitation (ST, grey lines) or with fixed 30 ka insolation (STI, black line). **f**, Summer (JJA) albedo changes from the same experiment (purple, shaded) and from the ST and STI experiments (grey and black lines). **g**, Scatter plot between the summer albedo changes in **f** (ref JJA) and the corresponding summer melt and the corresponding surface air temperature (shaded) over the same region. The time axis corresponds to the ice sheet model years.

transported from the Gulf of Mexico reaches the southern margin of the LIS, facilitating rapid ice sheet expansion by affecting both snow accumulation and ice melt via snow/ice–albedo feedback, with negligible effects due to transient changes of summer insolation in the northern high latitudes.

Furthermore, our model results indicate that the equilibrium state of the LIS is larger than an LGM-like configuration, which is consistent with the assumption that the LGM ice sheets are probably not representing an equilibrium solution but rather a transient state^{27,28}. Similarly, the rapid ice sheet expansion resulting from the proposed mechanism could effectively shorten the time for the LIS to reach the LGM-like configuration and further an equilibrium glacial maximum state. Additionally, we note that a decline in insolation and/or GHGs, along with the resultant cooling, are prerequisites for the self-adaptive mechanism-induced rapid growth to kick in. We further note that even though the self-adaptive mechanism drives the LIS towards a LGM configuration, the ice sheet geometry (at intermediate

ice sheet volumes) is a crucial element for millennial-scale abrupt events during MIS 3 under specific insolation and GHGs forcing conditions, for example, refs. 29–31. We highlight that aside from the Milankovitch control, the processes regulating the growth of ice sheets towards a glacial maximum state are more complex than previously assumed, which necessitates the use of complex Earth system models.

Although fully reconstructing the dynamics of ice sheet evolution from a geological perspective is challenging for the studied period, research focusing on specific regions offer partial insights. In particular, previous studies suggest a late build-up of the CIS–LIS saddle. The related reorganization of the ice drainage network in the southwest LIS (the shutdown/switch on of the related ice streams), the late local LGM of the northwest LIS and the subsequent migration of the Keewatin Ice Dome seems to be consistent with the experiment Tran_Paleomist^{32–35}. The hydrological features over North America at the LGM and the following deglaciation have been extensively investigated in

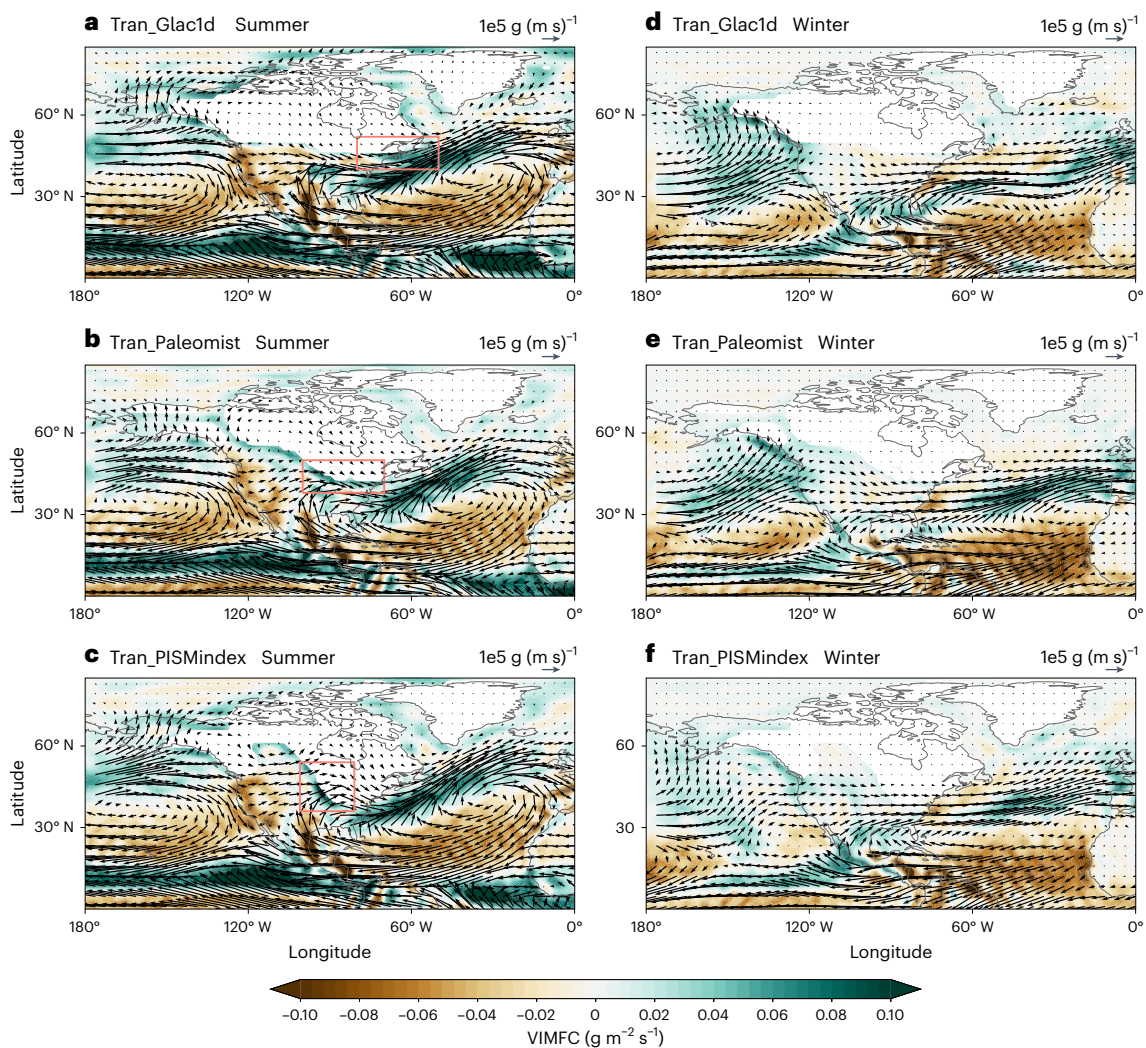


Fig. 5 | Vertically integrated moisture transportation and vertically integrated moisture flux convergence in summer and winter. a–c, Vertically integrated moisture transportation (vectors) when ice volumes of the LIS and the CIS are around 70 m SLE and the corresponding VIMFC (shaded) in summer

in experiment Tran_Glac1d (a), Tran_Paleomist (b) and Tran_PISMindex (c). **d–f,** Same as a–c but in winter. Pink boxes indicate areas with strong moisture transport on the ice sheets.

previous studies, with particular focus on the winter season^{36–42}. The presence of the continental-scale LIS rearranges the atmospheric circulation (for example, southward shifts of mid-latitude jet stream and/or storm track, southeast shift of North Pacific atmospheric rivers and zonalization of the North Atlantic jet at the LGM) and is found to dominate changes in the hydrological cycle^{43–45}. Our climate model in general shows consistent features with previous findings⁴⁶. Compared to winter, hydroclimate changes during summer have received less attention. Nevertheless, it has been proposed that a low-level southerly flow regime (from the Gulf of Mexico) that resembles a contemporary Great Plains low-level jet configuration is the primary route of moisture transport during summer⁴⁷. The presence of the LIS enhances the thermal gradient (baroclinicity) which favours the development of synoptic cyclones (increased moisture convergence by transient eddies) along the ice sheet margin at the LGM⁴⁵. Consistently, palaeoglacier reconstructions show lower east-side equilibrium-line altitudes in the southeastern Rocky Mountains, probably due to the increased Gulf moisture⁴⁸. Evidence from pluvial deposit and pedogenic carbonates in southwestern North America also suggest enhanced northward moisture transport during the presence of a large LIS^{49–51}. Our results indicate that the proposed regime may also exist during the period when the LIS grows from an intermediate size towards the LGM. More

importantly, we show that this is also the dominating factor in LIS development.

The low-level southerly flow is largely controlled by the orography of the North American continent, that is, the Rocky Mountains in the west and the southern margin of the LIS both constrain the northward moisture conveyor. This is different from the present day, where the large-scale LIS is absent. The mutual effects between the geometry of the LIS and the shape of the moisture conveyor finally result in self-adaptive LIS developments. Thus, a comprehensive GCM including explicit atmospheric dynamics and a sufficient spatial resolution to resolve LIS ice sheet margin heterogeneities is required to adequately simulate the ice sheet developments during this period. In addition, we emphasize the role of the ocean and air–sea coupling, which facilitates the water vapour transport from the subtropics (Extended Data Fig. 6). To test the importance of these interactions for specific ice volume trajectories in comparison to ice sheet reconstructions, future simulations with a synchronous ice sheet coupling are essential (Extended Data Fig. 7). Further investigations will also consider the Eurasian ice sheets, which show diverse responses in our different simulations, indicating that the mechanism for the Eurasian ice sheet development might be governed by different dynamics, for example, ref. 52.

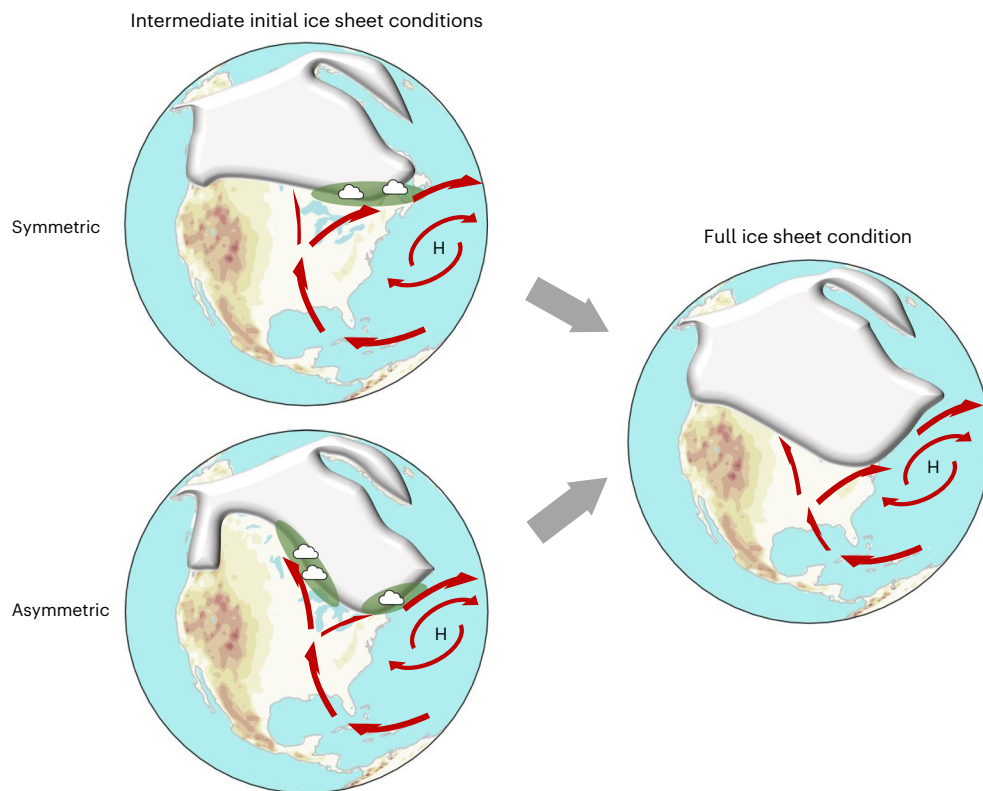


Fig. 6 | Cartoon of the proposed mechanism of the self-adaptive LIS. Red arrows indicate schematic summer moisture transport. H indicates Azores High in summer. Green shades are areas with large amount of precipitation. Basemap data from ref. 60.

Online content

Any methods, additional references, Nature Portfolio reporting summaries, source data, extended data, supplementary information, acknowledgements, peer review information; details of author contributions and competing interests; and statements of data and code availability are available at <https://doi.org/10.1038/s41561-024-01419-z>.

References

- Lisiecki, L. E., Raymo, M. E. A Pliocene–Pleistocene stack of 57 globally distributed benthic $\delta^{18}\text{O}$ records. *Paleoceanography* **20**, PA1003 (2005).
- Siddall, M., Rohling, E. J., Thompson, W. G. & Waelbroeck, C. Marine isotope stage 3 sea level fluctuations: data synthesis and new outlook. *Rev. Geophys.* **46**, RG4003 (2008).
- North Greenland Ice Core Project members. High-resolution record of Northern Hemisphere climate extending into the last interglacial period. *Nature* **431**, 147–151 (2004).
- Milankovitch, M. Kanon der Erdbestrahlung und seine Anwendung auf das Eiszeitenproblem. *Royal Serbian Academy Special Publication* **133**, 1–633 (1941).
- Berger, A. Long-term variations of daily insolation and Quaternary climatic changes. *J. Atmos. Sci.* **35**, 2362–2367 (1978).
- Lüthi, D. et al. High-resolution carbon dioxide concentration record 650,000–800,000 years before present. *Nature* **453**, 379–382 (2008).
- Bereiter, B. et al. Mode change of millennial CO_2 variability during the last glacial cycle associated with a bipolar marine carbon seesaw. *Proc. Natl Acad. Sci.* **109**, 9755–9760 (2012).
- Köhler, P., Nehrbass-Ahles, C., Schmitt, J., Stocker, T. F. & Fischer, H. A 156 kyr smoothed history of the atmospheric greenhouse gases CO_2 , CH_4 , and N_2O and their radiative forcing. *Earth Syst. Sci. Data* **9**, 363–387 (2017).
- Grant, K. M. et al. Rapid coupling between ice volume and polar temperature over the past 150,000 years. *Nature* **491**, 744–747 (2012).
- Bintanja, R., van de Wal, R. S. W. & Oerlemans, J. Modelled atmospheric temperatures and global sea levels over the past million years. *Nature* **437**, 125–128 (2005).
- Medina-Elizalde, M. A global compilation of coral sea-level benchmarks: implications and new challenges. *Earth Planet. Sci. Lett.* **362**, 310–318 (2013).
- Hasenclever, J. et al. Sea level fall during glaciation stabilized atmospheric CO_2 by enhanced volcanic degassing. *Nat. Commun.* **8**, 15867 (2017).
- Gowan, E. J. et al. A new global ice sheet reconstruction for the past 80,000 years. *Nat. Commun.* **12**, 1199 (2021).
- Kleman, J. et al. North American ice sheet build-up during the last glacial cycle, 115–21 kyr. *Quat. Sci. Rev.* **29**, 2036–2051 (2010).
- Stokes, C. R., Tarasov, L. & Dyke, A. S. Dynamics of the North American Ice Sheet Complex during its inception and build-up to the Last Glacial Maximum. *Quat. Sci. Rev.* **50**, 86–104 (2012).
- Dalton, A. S., Finkelstein, S. A., Barnett, P. J. & Forman, S. L. Constraining the Late Pleistocene history of the Laurentide Ice Sheet by dating the Missinaibi Formation, Hudson Bay Lowlands, Canada. *Quat. Sci. Rev.* **146**, 288–299 (2016).
- McMartin, I., Campbell, J. E. & Dredge, L. A. Middle Wisconsinan marine shells near Repulse Bay, Nunavut, Canada: implications for Marine Isotope Stage 3 ice-free conditions and Laurentide Ice Sheet dynamics in north-west Hudson Bay. *J. Quat. Sci.* **34**, 64–75 (2019).
- Pico, T., Creveling, J. & Mitrovica, J. Sea-level records from the U.S. mid-Atlantic constrain Laurentide Ice Sheet extent during Marine Isotope Stage 3. *Nat. Commun.* **8**, 15612 (2017).

19. Tarasov, L., Dyke, A. S., Neal, R. M. & Peltier, W. R. A data-calibrated distribution of deglacial chronologies for the North American ice complex from glaciological modeling. *Earth Planet. Sci. Lett.* **315**, 30–40 (2012).
20. Dalton, A. S. et al. Was the Laurentide Ice Sheet significantly reduced during Marine Isotope Stage 3? *Geology* **47**, 111–114 (2019).
21. Miller, G. H. & Andrews, J. T. Hudson Bay was not deglaciated during MIS-3. *Quat. Sci. Rev.* **225**, 105944 (2019).
22. Pico, T. Toward new and independent constraints on global mean sea-level highstands during the last glaciation (Marine Isotope Stage 3, 5a, and 5c). *Paleoceanogr. Paleoclimatol.* **37**, 2022–004560 (2022).
23. Abe-Ouchi, A., Segawa, T. & Saito, F. Climatic conditions for modelling the Northern Hemisphere ice sheets throughout the ice age cycle. *Clim. Past* **3**, 423–438 (2007).
24. Ganopolski, A., Calov, R. & Claussen, M. Simulation of the last glacial cycle with a coupled climate ice-sheet model of intermediate complexity. *Clim. Past* **6**, 229–244 (2010).
25. Ganopolski, A. & Brovkin, V. Simulation of climate, ice sheets and CO₂ evolution during the last four glacial cycles with an Earth system model of intermediate complexity. *Clim. Past* **13**, 1695–1716 (2017).
26. Löfverström, M., Liakka, J. & Kleman, J. The North American Cordillera—an impediment to growing the continent-wide Laurentide Ice Sheet. *J. Clim.* **28**, 9433–9450 (2015).
27. Ziemann, F., Rodehacke, C. & Mikolajewicz, U. Coupled ice sheet–climate modeling under glacial and pre-industrial boundary conditions. *Clim. Past* **10**, 1817–1836 (2014).
28. Abe-Ouchi, A. et al. Insolation-driven 100,000-year glacial cycles and hysteresis of ice-sheet volume. *Nature* **500**, 190–193 (2013).
29. Zhang, X. et al. Abrupt glacial climate shifts controlled by ice sheet changes. *Nature* **512**, 290–294 (2014).
30. Zhang, X. et al. Direct astronomical influence on abrupt climate variability. *Nat. Geosci.* **14**, 819–826 (2021).
31. Barker, S. & Knorr, G. Millennial scale feedbacks determine the shape and rapidity of glacial termination. *Nat. Commun.* **12**, 2273 (2021).
32. Margold, M., Stokes, C. R. & Clark, C. D. Reconciling records of ice streaming and ice margin retreat to produce a palaeogeographic reconstruction of the deglaciation of the Laurentide ice sheet. *Quat. Sci. Rev.* **189**, 1–30 (2018).
33. Kennedy, K., Froese, D., Zazula, G. & Lauriol, B. Last Glacial Maximum age for the northwest Laurentide maximum from the Eagle River spillway and delta complex, northern Yukon. *Quat. Sci. Rev.* **29**, 1288–1300 (2010).
34. Lacelle, D. et al. Timing of advance and basal condition of the Laurentide Ice Sheet during the last glacial maximum in the Richardson Mountains, NWT. *Quat. Res.* **80**, 274–283 (2013).
35. Stoker, B. J. et al. The collapse of the Cordilleran–Laurentide ice saddle and early opening of the Mackenzie Valley, Northwest Territories, Canada, constrained by ¹⁰Be exposure dating. *Cryosphere* **16**, 4865–4886 (2022).
36. McGee, D. Glacial–interglacial precipitation changes. *Annu. Rev. Mar. Sci.* **12**, 525–557 (2020).
37. Manabe, S. & Broccoli, A. The influence of continental ice sheets on the climate of an ice age. *J. Geophys. Res.: Atmos.* **90**, 2167–2190 (1985).
38. Bartlein, P. J. et al. Paleoclimate simulations for North America over the past 21,000 years: features of the simulated climate and comparisons with paleoenvironmental data. *Quat. Sci. Rev.* **17**, 549–585 (1998).
39. Kageyama, M. & Valdes, P. J. Impact of the North American ice-sheet orography on the Last Glacial Maximum eddies and snowfall. *Geophys. Res. Lett.* **27**, 1515–1518 (2000).
40. Lora, J. M., Mitchell, J. L., Risi, C. & Tripathi, A. E. North Pacific atmospheric rivers and their influence on western North America at the Last Glacial Maximum. *Geophys. Res. Lett.* **44**, 1051–1059 (2017).
41. Merz, N., Raible, C. C. & Woollings, T. North Atlantic eddy-driven jet in interglacial and glacial winter climates. *J. Clim.* **28**, 3977–3997 (2015).
42. Löfverström, M., Caballero, R., Nilsson, J. & Messori, G. Stationary wave reflection as a mechanism for zonalizing the Atlantic winter jet at the LGM. *J. Atmos. Sci.* **73**, 3329–3342 (2016).
43. Cook, K. H. & Held, I. M. Stationary waves of the ice age climate. *J. Clim.* **1**, 807–819 (1988).
44. Löfverström, M. & Lora, J. M. Abrupt regime shifts in the North Atlantic atmospheric circulation over the last deglaciation. *Geophys. Res. Lett.* **44**, 8047–8055 (2017).
45. Lora, J. M. Components and mechanisms of hydrologic cycle changes over North America at the last glacial maximum. *J. Clim.* **31**, 7035–7051 (2018).
46. Kageyama, M. et al. The PMIP4 last glacial maximum experiments: preliminary results and comparison with the PMIP3 simulations. *Clim. Past* **17**, 1065–1089 (2021).
47. Bromwich, D. H., Toracinta, E. R., Oglesby, R. J., Fastook, J. L. & Hughes, T. J. LGM summer climate on the southern margin of the Laurentide ice sheet: wet or dry? *J. Clim.* **18**, 3317–3338 (2005).
48. Refsnider, K. A., Brugger, K. A., Leonard, E. M., McCALPIN, J. P. & Armstrong, P. P. Last glacial maximum equilibrium-line altitude trends and precipitation patterns in the Sangre de Cristo Mountains, southern Colorado, USA. *Boreas* **38**, 663–678 (2009).
49. Wells, P. V. An equable glaciopluvial in the west: pleniglacial evidence of increased precipitation on a gradient from the Great Basin to the Sonora and Chihuahuan deserts. *Quat. Res.* **12**, 311–325 (1979).
50. Amundson, R., Chadwick, O., Kendall, C., Wang, Y. & DeNiro, M. Isotopic evidence for shifts in atmospheric circulation patterns during the late Quaternary in mid-North America. *Geology* **24**, 23–26 (1996).
51. Oerter, E. J. et al. Pedothem carbonates reveal anomalous North American atmospheric circulation 70,000–55,000 years ago. *Proc. Natl Acad. Sci.* **113**, 919–924 (2016).
52. Löfverström, M., Thompson, D. M., Otto-Bliesner, B. L., Brady, E. C. The importance of Canadian Arctic Archipelago gateways for glacial expansion in Scandinavia. *Nat. Geosci.* **15**, 482–488 (2022).
53. Peltier, W. R., Argus, D. & Drummond, R. Space geodesy constrains ice age terminal deglaciation: the global ICE-6G_C (VM5a) model. *J. Geophys. Res.: Solid Earth* **120**, 450–487 (2015).
54. Batchelor, C. L. et al. The configuration of Northern Hemisphere ice sheets through the Quaternary. *Nat. Commun.* **10**, 3713 (2019).
55. Yokoyama, Y., Esat, T. M. & Lambeck, K. Coupled climate and sea-level changes deduced from Huon Peninsula coral terraces of the last ice age. *Earth Planet. Sci. Lett.* **193**, 579–587 (2001).
56. de Gelder, G. et al. High interstadial sea levels over the past 420 ka from the Huon Peninsula, Papua New Guinea. *Commun. Earth Environ.* **3**, 256 (2022).
57. Waelbroeck, C. et al. Sea-level and deep water temperature changes derived from benthic foraminifera isotopic records. *Quat. Sci. Rev.* **21**, 295–305 (2002).
58. Spratt, R. M. & Lisiecki, L. E. A late Pleistocene sea level stack. *Clim. Past* **12**, 1079–1092 (2016).
59. Weiss, T. L., Linsley, B. K., Gordon, A. L., Rosenthal, Y. & Dannenmann-Di Palma, S. Constraints on Marine Isotope Stage 3 and 5 sea level from the flooding history of the Karimata Strait in Indonesia. *Paleoceanogr. Paleoclimatol.* **37**, 2021–004361 (2022).
60. Amante, C., Eakins, B. W. *ETOPO11 Arc-Minute Global Relief Model: Procedures, Data Sources and Analysis* NOAA Technical Memorandum NESDIS NGDC-24 (National Geophysical Data Center, NOAA, 2009).

Publisher's note Springer Nature remains neutral with regard to jurisdictional claims in published maps and institutional affiliations.

Open Access This article is licensed under a Creative Commons Attribution 4.0 International License, which permits use, sharing, adaptation, distribution and reproduction in any medium or format, as long as you give appropriate credit to the original author(s) and the source, provide a link to the Creative Commons licence, and indicate if changes were made. The images or other third party material in this

article are included in the article's Creative Commons licence, unless indicated otherwise in a credit line to the material. If material is not included in the article's Creative Commons licence and your intended use is not permitted by statutory regulation or exceeds the permitted use, you will need to obtain permission directly from the copyright holder. To view a copy of this licence, visit <http://creativecommons.org/licenses/by/4.0/>.

© The Author(s) 2024

Methods

Earth system model AWI-ESM with interactive ice sheets

Here we apply the state-of-the-art Earth system model (AWI-ESM, version 2.1) asynchronously coupled to the Parallel Ice Sheet Model (PISM, version 1.2). AWI-ESM-2.1 includes the global General Circulation Model (GCM) ECHAM6 for the atmosphere and land surface components and FESOM2 for the sea ice–ocean component⁶¹. ECHAM6 is the sixth generation of the ECHAM atmospheric GCM⁶². Driven by radiative forcing, it incorporates diabatic processes with large-scale circulations. The dynamic core of ECHAM6 is based on the vorticity and divergence form of the primitive equations, and thermodynamic coordinates are with temperature and surface pressure. Compared with previous versions, an improved radiative transfer scheme (RRTM-G) for both shortwave and longwave spectrum is applied⁶³. The representations of surface albedo over land and ocean are also substantially improved. Besides, an optimized dynamic vegetation model JSBACH that accounts for the land processes is also included. The resolution is T63 (–1.9°) on a Gaussian grid, with 47 vertical levels extending up to 0.01 hPa of the atmosphere. For ECHAM6, representation of tropical variability and improved performance in the circulation over mid-latitudes are remarkable⁶². FESOM2 (Finite-volume Sea ice–Ocean Model) resolves global sea ice–ocean characteristics on an unstructured mesh with multi-resolution modelling functionality⁶⁴. It uses the linear free surface scheme to account for surface freshwater fluxes in which a virtual salinity flux is introduced as an additional surface boundary condition. The resolution ranges spatially from 20 km over dynamically active regions to 140 km elsewhere. The flux exchanges between ECHAM6 and FESOM2 are conducted via OASIS3-MCT. AWI-ESM-2.1 has been used for palaeoclimate simulations at different time slices and is also part of the Paleoclimate Modelling Intercomparison Project 4 (PMIP4)^{46,65,66}. The model shows comparable performances as other PMIP4 models for the LGM. When applied to the mid-Holocene and the last interglacial, good performances are also shown in insolation driven seasonality variations, intertropical convergence zone/Northern Hemisphere Hadley circulation shifts and Northern Hemisphere summer monsoon intensification⁶⁵.

The ice sheet model PISM is a three-dimensional thermo-mechanically coupled shallow ice sheet model⁶⁷. The hybrid shallow ice approximation and shallow shelf approximation are used for computing the stress balance. For ice deformation, the enthalpy-based Glen–Paterson–Budd–Liboutry–Duval law is used^{68–70}. Enhancement factors of 5.0 and 0.5 are added to shallow ice approximation and shallow shelf approximation, respectively. For the bedrock deformation underneath the ice sheets, the Lingle–Clark scheme is used^{71,72}. The spatial resolution of the model domain is 20 km, with a Northern Hemisphere polar stereographic projection. PISM applies a boundary surface interface between top-ice-surface and firn layers. The interface covers ice surfaces and all other grounded areas. Top-ice-surface temperature and climatic surface mass balance that is calculated from a separated surface energy balance model is used as input for PISM. The ice mask is selected based on a threshold ice thickness of 0.5 m. The PICO scheme is used for ocean-induced melting below ice shelves. For the ice sheet spin-up, a heuristic scheme is applied to determine the temperatures at depth (using ice thickness, surface temperature, surface mass balance and geothermal flux), which is a solution of a steady one-dimensional differential equation, and vertical velocity is linearly interpolated based on the surface mass balance⁶⁷.

A notable feature of the coupled model set-up is the application of an advanced surface mass balance scheme dEBM (diurnal energy balance model)⁷³. Most of previous ice sheet simulations have used the semi-empirical positive degree-day scheme, which only takes surface air temperature into account for surface melt, for example, ref. 27. The positive degree-day scheme is often calibrated based on modern observations from the Greenland Ice Sheet, which appears not suitable for the glacial ice sheets with substantially different background climate

and radiative forcing^{74–76}. The dEBM scheme used here accounts for changes in the Earth's orbit and atmospheric composition, implicitly accounts for the diurnal melt–freeze cycle and uses physics-based, non-empirical parameters. Only the albedo scheme has been calibrated specifically for today's Greenland surface mass balance: it distinguishes three surface types with distinct albedo values $A_{f,c}$ for fair and cloudy conditions: new snow ($A_{f,c} = \{0.845, 0.895\}$), dry snow ($A_{f,c} = \{0.73, 0.78\}$) and wet snow or bare ice ($A_{f,c} = \{0.55, 0.6\}$). The classification of surface types is conducted based on energy balance, accumulation and snow height. The dEBM scheme is particularly suitable for palaeo simulations because it is computationally inexpensive and requires only monthly input (that is, near-surface temperature, precipitation, cloud cover, short- and longwave radiation).

Asynchronous coupling is conducted between the climate components and the ice sheets. Due to the computational limits coming from the relatively high-resolution GCM (approximately 50 model years per day on the German Climate Computing Center (Deutsches Klimarechenzentrum, DKRZ) supercomputer), an acceleration factor of 20 is applied (five climate model years vs 100 ice sheet model years). The acceleration factor has been tested both in simple flowline models and more complex models under equilibrium conditions^{77,78}. A coupling cycle consists of four phases: (1) the AWI-ESM-2.1 is first integrated for five years for a given ice sheet configuration. (2) The climate model output is then used to generate forcing for the ice sheet model PISM: multiyear mean ocean temperature and salinity at the ice–ocean boundary and the SMB at the surface as calculated by dEBM from monthly atmospheric forcing. (3) The ice sheet model PISM is integrated for 100 years. (4) Finally, to complete the coupling cycle, the simulated ice sheet state provides new boundary conditions for the climate model. Ice mass changes are translated into respective freshwater discharges and are transferred via a hydrology model to the nearest coasts, and changes in ice mask and orography are communicated to the atmospheric component. As such, the simulations between AWI-ESM and PISM are switched back and forth. To be noted, the bathymetry in FESOM2 is fixed at 38 ka condition, because change of bathymetry on an unstructured mesh is currently not technically applicable. The influence of bathymetry changes on our conclusion is considered to be minor, because the North American ice sheets are mostly land based. The coupling between the climate and the ice sheets are applied to the Northern Hemisphere, whereas the Antarctic ice sheet is kept fixed at 38 ka.

Experimental details

Three ice sheet configurations during MIS 3 (around 38 ka) are used as initial conditions (Fig. 1b–d): two are from two palaeo-ice sheet reconstructions of GlacID¹⁹ and Paleomist¹³ and one is from a standalone ice sheet simulation using the glacial index method (PISM-index, derived from the LGM and present-day climates from AWI-ESM). The GlacID and Paleomist datasets are based on geophysical modelling of glacial isostatic adjustment (GIA) processes and are partially constrained by far-field/local relative sea level and geological observations. The ice coverage from GlacID-38k is extensive, where the southwestern margin of the ice sheet almost reaches to the LGM extent. Contrarily, the ice sheet from Paleomist-38k is considerably reduced. In the one from PISM-index-38k, more ice is present over southeast of the ice sheet. This is probably because the glacial index method generates the climate forcing from composites of two climate states (LGM and present day), where the LGM state introduce intensified precipitation over the southeastern margin of the corresponding LGM ice sheet, whereas precipitation over its west and interior are almost absent.

In the reference transient simulations, perturbations of freshwater (0.3 Sv) are imposed into the Ruddiman belt after 32 ka to mimic a weaker than the modern Atlantic meridional overturning circulation (AMOC) state (Fig. 1a). To test the development of LIS in the face of a relatively strong AMOC, we have also conducted sensitivity experiments

without freshwater perturbations. The characteristics of simulated climate responses between strong and weak AMOC states align with proxy-based reconstructions of climate fluctuations of Dansgaard–Oeschger oscillations (DOs) (Extended Data Fig. 6). The growth rate of the LIS is largely impeded when compared with weakened AMOC mode, not only due to higher surface temperature over North America but also reduced moisture transport from the Gulf of Mexico (Extended Data Fig. 6). Although the explicit succession of abrupt millennial timescale events are not captured in our simulations⁷⁹, the results suggest that in our model configuration, the dominant growth mode arises from stadial (that is, rather weak) AMOC conditions (Extended Data Fig. 7, black and grey lines). For our study, higher acceleration factor of 100 is also tested for transient and fixed 21 k scenarios (Extended Data Fig. 7, red and blue lines). The reorganization of atmospheric circulation is mainly orographically controlled and is independent of the acceleration factors.

To deduce the effect of summer snowfall, a sensitivity test on the SMB (ST) is conducted. In the ST experiment, summer (JJA) snowfall is reduced to the winter (DJF) amount, whereas all other variables are kept unchanged, and then the SMB over time is recalculated using dEBM. The newly calculated total SMB, accumulation (snow and refreeze), melt and surface albedo are indicated in grey lines in Fig. 4e,f. To test the direct role of decreasing summer insolation (incoming shortwave radiation) on the SMB, we conducted another sensitivity test (STI). In this experiment, we fix the insolation at 30 ka, whereas all other variables are kept unchanged, and then recalculate the SMB using dEBM. The newly calculated total SMB and surface albedo is illustrated in black lines in Fig. 4e,f. This STI experiment (together with a further sensitivity test with solely varying insolation but fixed all other variables at 30 ka) confirms that the direct contribution of insolation on the SMB after 30 ka is negligible, highlighting the importance of internal climate dynamics towards the establishment of full LGM ice sheet conditions.

Model–data comparison

In Fig. 1h, the simulated ice volume changes of the NA ice sheets are compared with global mean sea level estimates or relative sea level observations based on corals^{11,55,56}, foraminiferal oxygen isotopes^{57–59}, or glacial isostatic adjustment (GIA) models^{13,18} (dots/dotted lines). Note that the decreases in reconstructed global/relative sea levels during this period also account for changes of the Eurasian ice sheets (EIS) and the Antarctic Ice Sheet. However, before -30 ka, the extents of the EIS were very limited (sea level equivalent ice volume was less than 5 m) and mainly restricted in the mountainous areas^{13,19,54}. From -30 ka to 21 ka, expansions of the EIS happened, with increased sea level equivalent ice volume around 15 m. For the contribution of Antarctic ice sheet to global sea level, large uncertainties prior to the LGM still exist, which varies between 5 and 22 m (ref. 54). Sea level contribution from Greenland ice sheet during this period is rather negligible (around 1 m). Furthermore, changes in ice volume of the NA ice sheets are also compared to estimates based on ice extent reconstructions (purple error bars). The related ice volumes are calculated using a simple area–volume scaling relationship⁵⁴: $V = cA^y$. The scaling exponent y is 1.25 (ref. 80). The coefficient c is derived from output of ice sheet modelling in this study for the NAIS ($c = 0.03233$). In general, our simulated ice volume changes show a good match with the reconstructions. In particular, the simulated ice volume changes from Tran_Paleomist match very well with the ice extent derived estimations (purple error bars). These add credibility to our proposed mechanism for explaining the rapid ice sheet expansions.

A model–data comparison in terms of the ocean state is also conducted. During MIS 3, millennial-scale abrupt climate shifts occurred, with which transitions between weak AMOC states and warm AMOC states happened. Here we compare our results with different published records to assess the reliability of different AMOC states³⁰ (Extended Data Fig. 6). From the figure, we see that the characteristics of simulated

climate responses between strong and weak AMOC states align with proxy-based reconstructions of climate fluctuations of DOs. Our model shows good performance during MIS 3, and it is comparable to other climate models^{30,81,82}. In our simulations, the global annual mean surface temperatures (at approximately 33 ka) are 3.0 °C, 2.6 °C and 2.7 °C cooler than the pre-industrial (PI) state for Tran_GlacId, Tran_Paleomist, Tran_PISMindex, respectively. The magnitude of this temperature difference is similar to the cooling in other studies^{81,82}.

Data availability

The reconstructed palaeo records, including ice core, CO₂ levels, global/relative sea levels and ice sheet reconstructions, are available through the referenced sources. The AWI-ESM model data discussed in this study are available via Zenodo at <https://doi.org/10.5281/zenodo.10646880> (ref. 83).

Code availability

The AWI Earth System Model (AWI-ESM, version 2.1) consists of the atmospheric component ECHAM6 (including land surface scheme JSBACH) and the ocean–sea ice component FESOM (<https://fesom.de/models/awi-esm/>). The ECHAM6 model is distributed by the Max Planck Institute for Meteorology in Hamburg and is available upon request. A modified version can be found at: <https://gitlab.awi.de/paleodyn/Models/echam6>. The source code of the FESOM2 model is available to the public via Github at <https://github.com/FESOM/fesom2> (ref. 84). The Parallel Ice Sheet Model PISM is available via Github at <https://github.com/pism/pism> (ref. 85). The coupling between the climate model and the ice sheet model is conducted via ESM-Tools from Github at https://github.com/esm-tools/esm_tools (ref. 86).

References

- Sidorenko, D. et al. Evaluation of FESOM2.0 coupled to ECHAM6.3: preindustrial and highresmp simulations. *J. Adv. Model. Earth Syst.* **11**, 3794–3815 (2019).
- Stevens, B. et al. Atmospheric component of the MPI-M Earth system model: ECHAM6. *J. Adv. Model. Earth Syst.* **5**, 146–172 (2013).
- Iacono, M. J. et al. Radiative forcing by long-lived greenhouse gases: calculations with the AER radiative transfer models. *J. Geophys. Res.: Atmos.* **113**, D13103 (2008).
- Scholz, P. et al. Assessment of the Finite-volume Sea ice–Ocean Model (fesom2.0)–part 1: description of selected key model elements and comparison to its predecessor version. *Geosci. Model Dev.* **12**, 4875–4899 (2019).
- Shi, X., Werner, M., Wang, Q., Yang, H. & Lohmann, G. Simulated mid-Holocene and last interglacial climate using two generations of AWI-ESM. *J. Clim.* **35**, 7811–7831 (2022).
- Hossain, A. et al. The impact of different atmospheric CO₂ concentrations on large scale Miocene temperature signatures. *Paleoceanogr. Paleoclimatol.* **38**, 2022–004438 (2023).
- Bueler, E. & Brown, J. Shallow shelf approximation as a “sliding law” in a thermomechanically coupled ice sheet model. *J. Geophys. Res. Earth Surf.* **114**, F03008 (2009).
- Paterson, W. & Budd, W. Flow parameters for ice sheet modeling. *Cold Reg. Sci. Technol.* **6**, 175–177 (1982).
- Lliboutry, L. & Duval, P. Various isotropic and anisotropic ices found in glaciers and polar ice caps and their corresponding rheologies. *Ann. Geophys.* **3**, 207–224 (1985).
- Aschwanden, A., Bueler, E., Khroulev, C. & Blatter, H. An enthalpy formulation for glaciers and ice sheets. *J. Glaciol.* **58**, 441–457 (2012).
- Lingle, C. S. & Clark, J. A. A numerical model of interactions between a marine ice sheet and the solid earth: application to a West Antarctic ice stream. *J. Geophys. Res. Oceans* **90**, 1100–1114 (1985).

72. Bueler, E., Lingle, C. S. & Brown, J. Fast computation of a viscoelastic deformable Earth model for ice-sheet simulations. *Ann. Glaciol.* **46**, 97–105 (2007).
73. Krebs-Kanzow, U. et al. The diurnal Energy Balance Model (dEBM): a convenient surface mass balance solution for ice sheets in Earth system modeling. *Cryosphere* **15**, 2295–2313 (2021).
74. Reeh, N. Parameterization of melt rate and surface temperature in the Greenland ice sheet. *Polarforschung* **59**, 113–128 (1991).
75. Van de Berg, W. J., Van Den Broeke, M., Ettema, J., Van Meijgaard, E. & Kaspar, F. Significant contribution of insolation to Eemian melting of the Greenland ice sheet. *Nat. Geosci.* **4**, 679–683 (2011).
76. Plach, A. et al. Eemian Greenland SMB strongly sensitive to model choice. *Clim. Past* **14**, 1463–1485 (2018).
77. Pollard, D., Muszynski, I., Schneider, S. H. & Thompson, S. L. Asynchronous coupling of ice-sheet and atmospheric forcing models. *Ann. Glaciol.* **14**, 247–251 (1990).
78. Niu, L., Lohmann, G., Gierz, P., Gowan, E. J. & Knorr, G. Coupled climate-ice sheet modelling of MIS-13 reveals a sensitive Cordilleran ice sheet. *Glob. Planet. Change* **200**, 103474 (2021).
79. Niu, L., Lohmann, G. & Gowan, E. J. Climate noise influences ice sheet mean state. *Geophys. Res. Lett.* **46**, 9690–9699 (2019).
80. Cuffey, K. M., Paterson, W. S. B. *The Physics of Glaciers* (Academic Press, 2010).
81. Guo, C., Nisancioglu, K. H., Bentsen, M., Bethke, I. & Zhang, Z. Equilibrium simulations of Marine Isotope Stage 3 climate. *Clim. Past* **15**, 1133–1151 (2019).
82. Zhang, X., Prange, M., Merkel, U. & Schulz, M. Instability of the Atlantic overturning circulation during Marine Isotope Stage 3. *Geophys. Res. Lett.* **41**, 4285–4293 (2014).
83. Niu, L. et al. Laurentide Ice Sheet evolution towards the Last Glacial Maximum using AWIESM model with interactive ice sheets. *Zenodo* <https://doi.org/10.5281/zenodo.10646880> (2024).
84. Danilov, S., Sidorenko, D., Wang, Q. & Jung, T. The Finite-volume Sea ice–Ocean Model (FESOM2). *Zenodo* <https://doi.org/10.5281/zenodo.161319> (2016).
85. Khrulev, C. et al. Parallel Ice Sheet Model (PISM). *Zenodo* <https://doi.org/10.5281/zenodo.1199019> (2023).
86. Miguel, A. et al. esm-tools/esm_tools: Release 6 (v6.0.0). *Zenodo* <https://doi.org/10.5281/zenodo.5787476> (2021).

Acknowledgements

We thank colleagues at both the Alfred Wegener Institute Helmholtz Center for Polar and Marine Research (AWI) in

Bremerhaven (Germany) and other institutes for helpful discussions. This study is supported by the German Federal Ministry of Education and Research (BMBF) funded project PalMod (grant numbers O1LP1915A and O1LP2303A to G.K. and O1LP1916B to G.L.) and contributes to the Helmholtz research programme ‘Changing Earth—Sustaining our Future’ and the Helmholtz Climate Initiative ‘REKLIM’. The development of PISM is supported by the National Aeronautics and Space Administration (NASA) grant NNX17AG65G and the National Science Foundation (NSF) grants PLR-1603799 and PLR-1644277. We thank the Max Planck Institute in Hamburg and colleagues from the AWI for making ECHAM6-JSBACH and FESOM2 available. Computational resources were made available by the infrastructure and support of the computing centre of the AWI in Bremerhaven and the DKRZ in Hamburg, Germany.

Author contributions

L.N. and G.K. designed the work. L.N. performed the Earth system modelling experiments and the analysis. L.N. wrote the paper with help of G.K. L.N., G.K., U.K.-K. and G.L. contributed to the interpretation and discussion of the results. All authors provided input to the final version of the manuscript.

Funding

Open access funding provided by Alfred-Wegener-Institut.

Competing interests

The authors declare no competing interests.

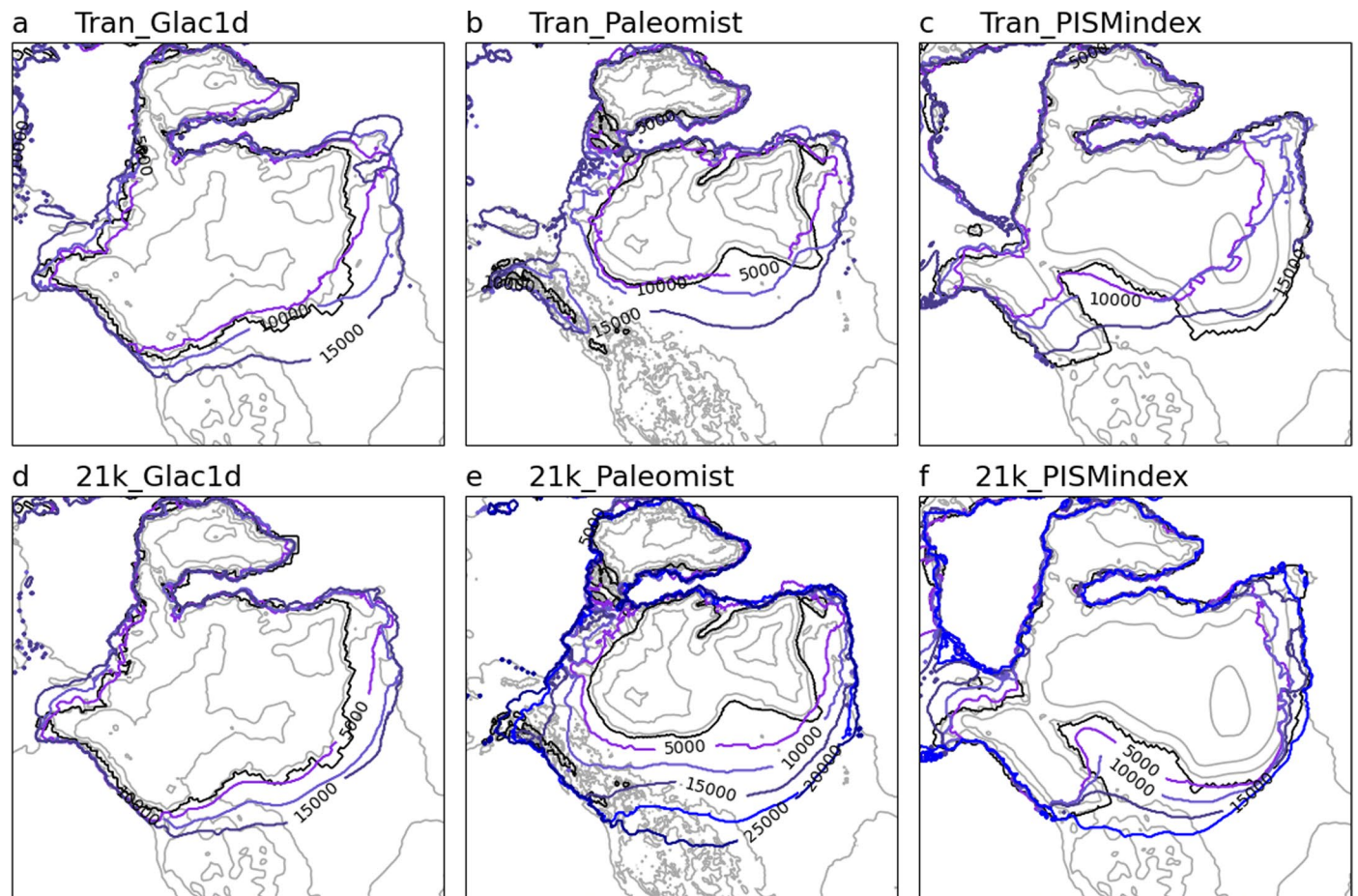
Additional information

Extended data is available for this paper at <https://doi.org/10.1038/s41561-024-01419-z>.

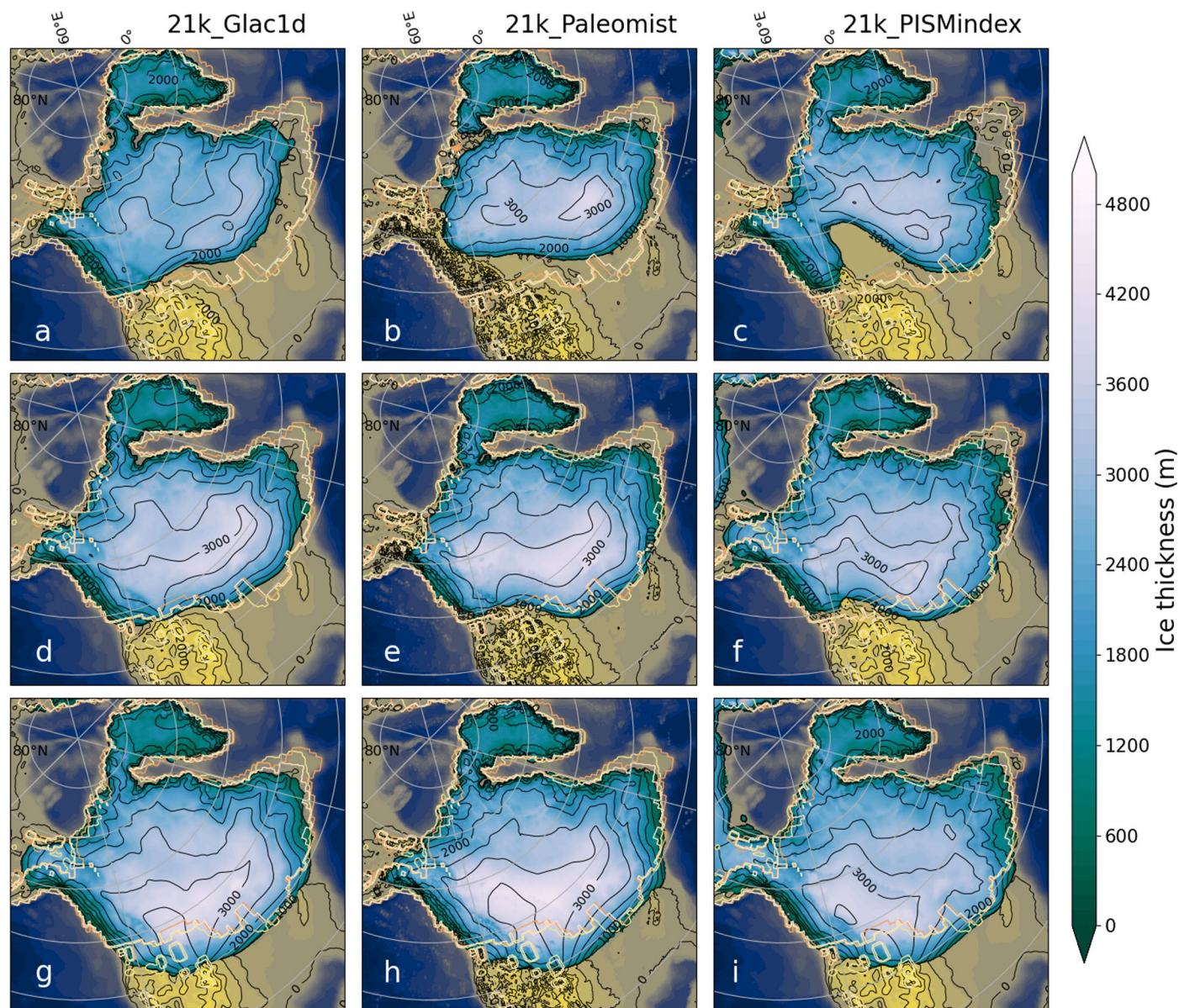
Correspondence and requests for materials should be addressed to Lu Niu.

Peer review information *Nature Geoscience* thanks Martin Margold and the other, anonymous, reviewer(s) for their contribution to the peer review of this work. Primary Handling Editor: James Super, in collaboration with the *Nature Geoscience* team.

Reprints and permissions information is available at www.nature.com/reprints.

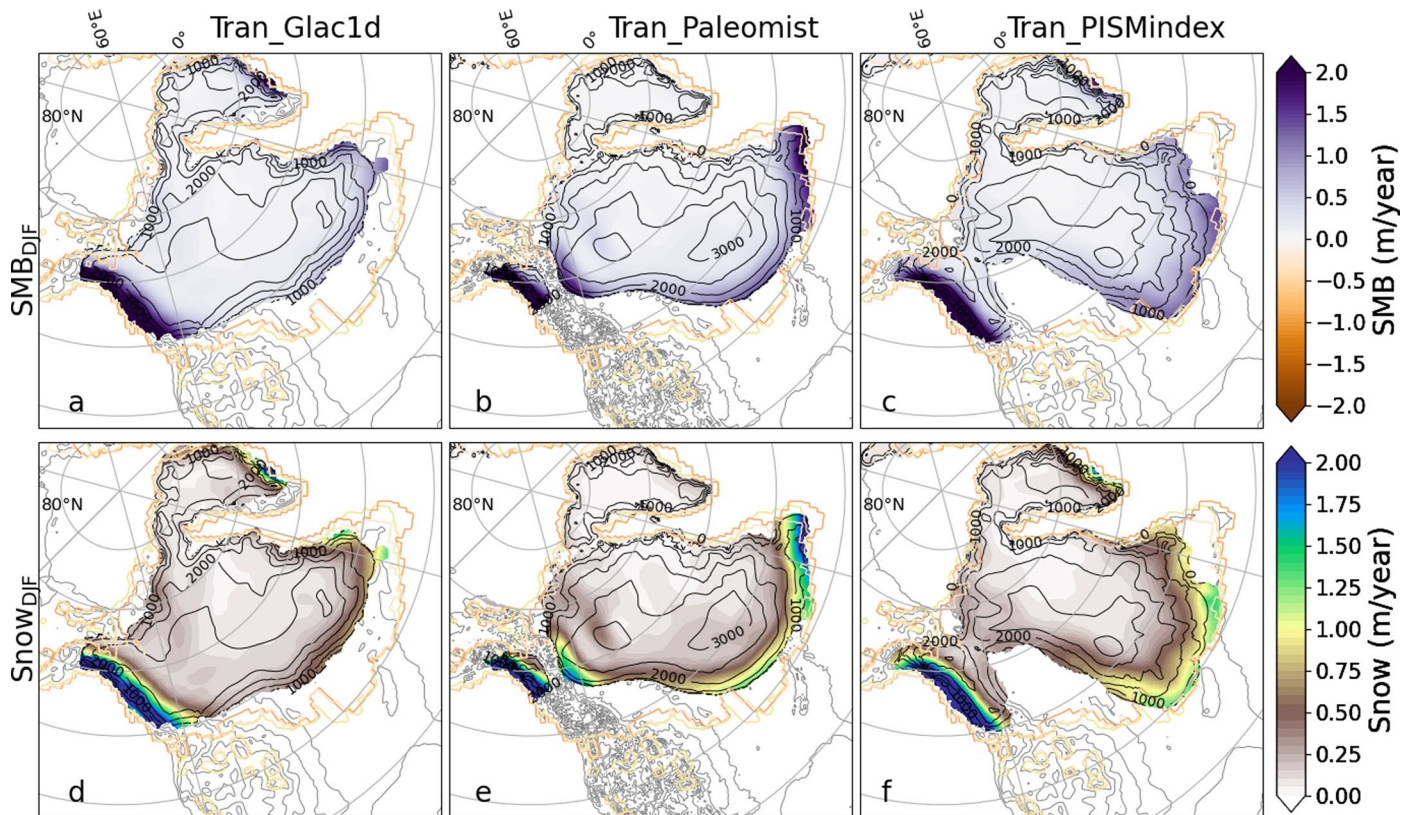


Extended Data Fig. 1 | Spatial evolution of simulated North American ice sheets. Changes in ice sheet extents under transient orbital and Greenhouse gases (GHGs) forcing in every 5000 ice sheet model years, initialized from ice sheet configurations at 38 ka from **a)** Glac1D, **b)** Paleomist and **c)** PISM-index, respectively. **d-f)** same as in **a-c)**, but with fixed 21 ka orbital and GHGs forcing.



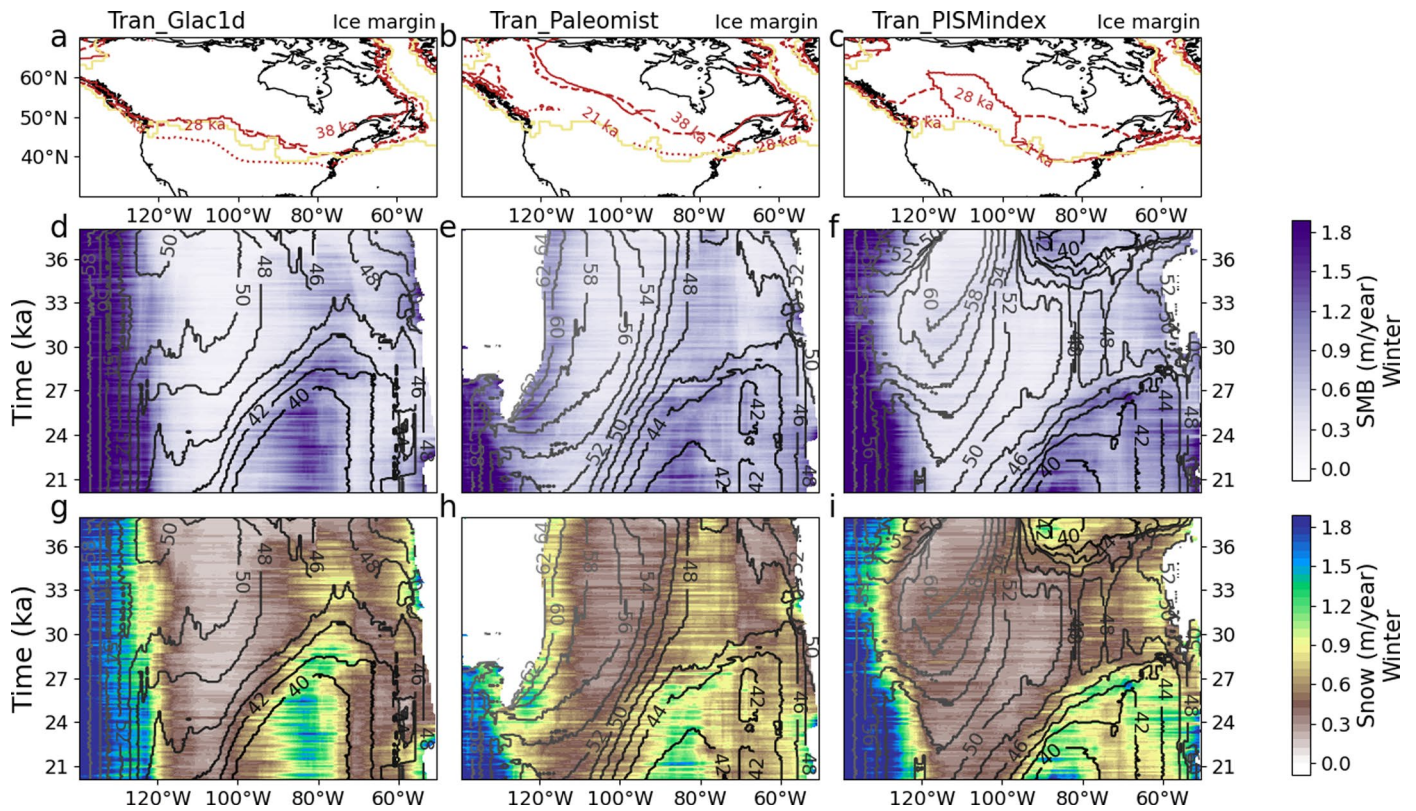
Extended Data Fig. 2 | Ice thickness patterns of North American ice sheets at different ice volumes in experiments with fixed 21k orbital and Greenhouse gas forcing. Ice thickness distributions when the ice volume of the North American ice sheets (excluding Greenland ice sheet) reaches 70 m in Sea Level Equivalent (SLE) for experiment **a**) 21k_Glac1d, **b**) 21k_Paleomist and **c**) 21k_

PISMindex. **d-f**) same as **a-c**, but for 100 m SLE. **g-i**) same as **a-c**, but for 120 m SLE. Black contours depict surface elevation with a 500 m interval. Yellowish contours represent reconstructed ice sheet extents from different reconstruction datasets (Glac1D, Paleomist and Ice6g) at 21 ka.



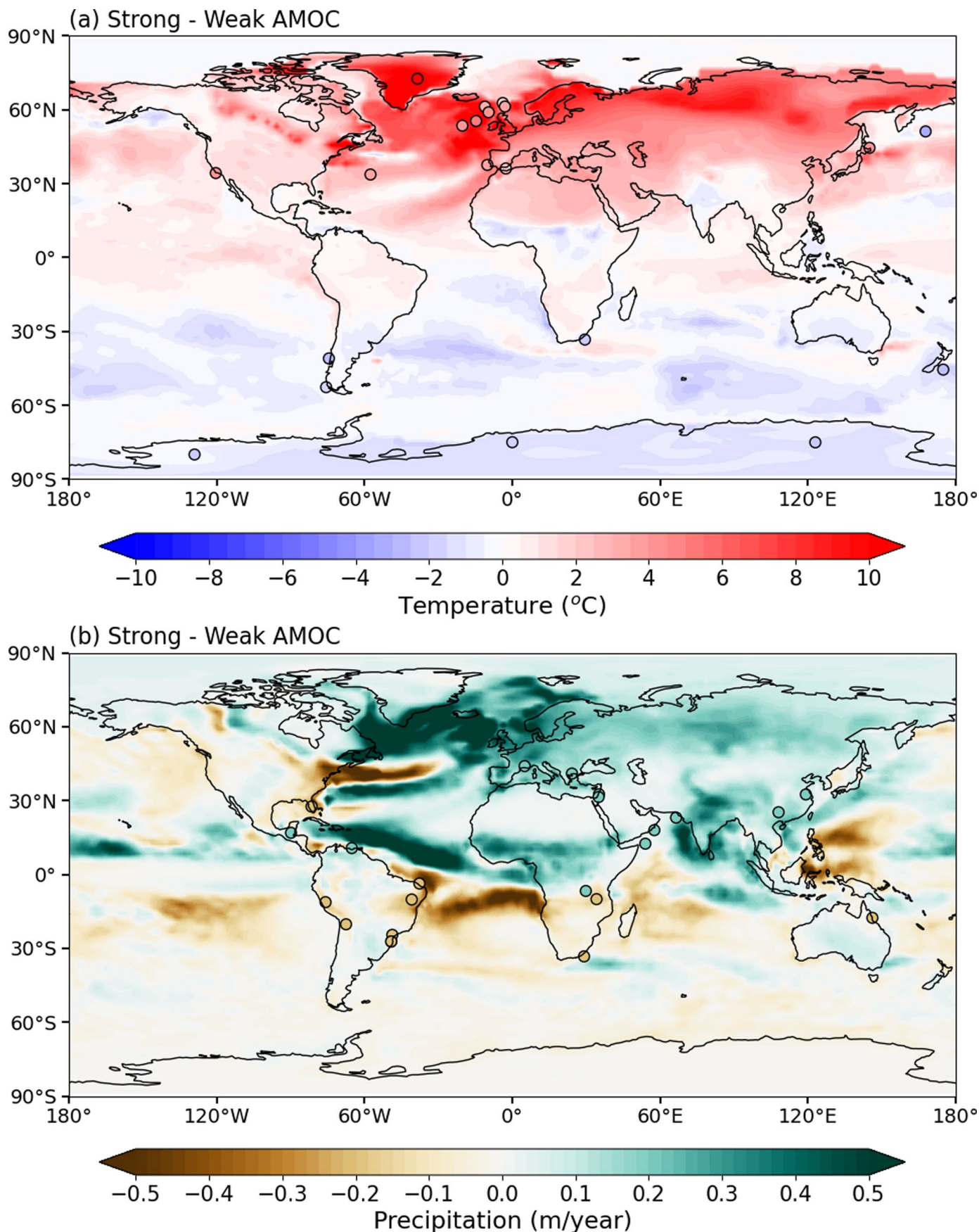
Extended Data Fig. 3 | Simulated surface mass balance and snowfall in winter with North American ice sheets at intermediate states. Surface mass balance (SMB) over ice sheets in winter (DJF) with ice sheets at intermediate states (70 m SLE) from different experiments: **a)** Tran_Glac1d, **b)** Tran_Paleomist, **c)**

Tran_PISMindex. **d-f)** Same as **a-c**, but for snowfall. Black contours depict surface elevation with a 500 m interval. Yellowish contours represent reconstructed ice sheet extents from different datasets (Glac1D, Paleomist, and Ice6g) at 21 ka.



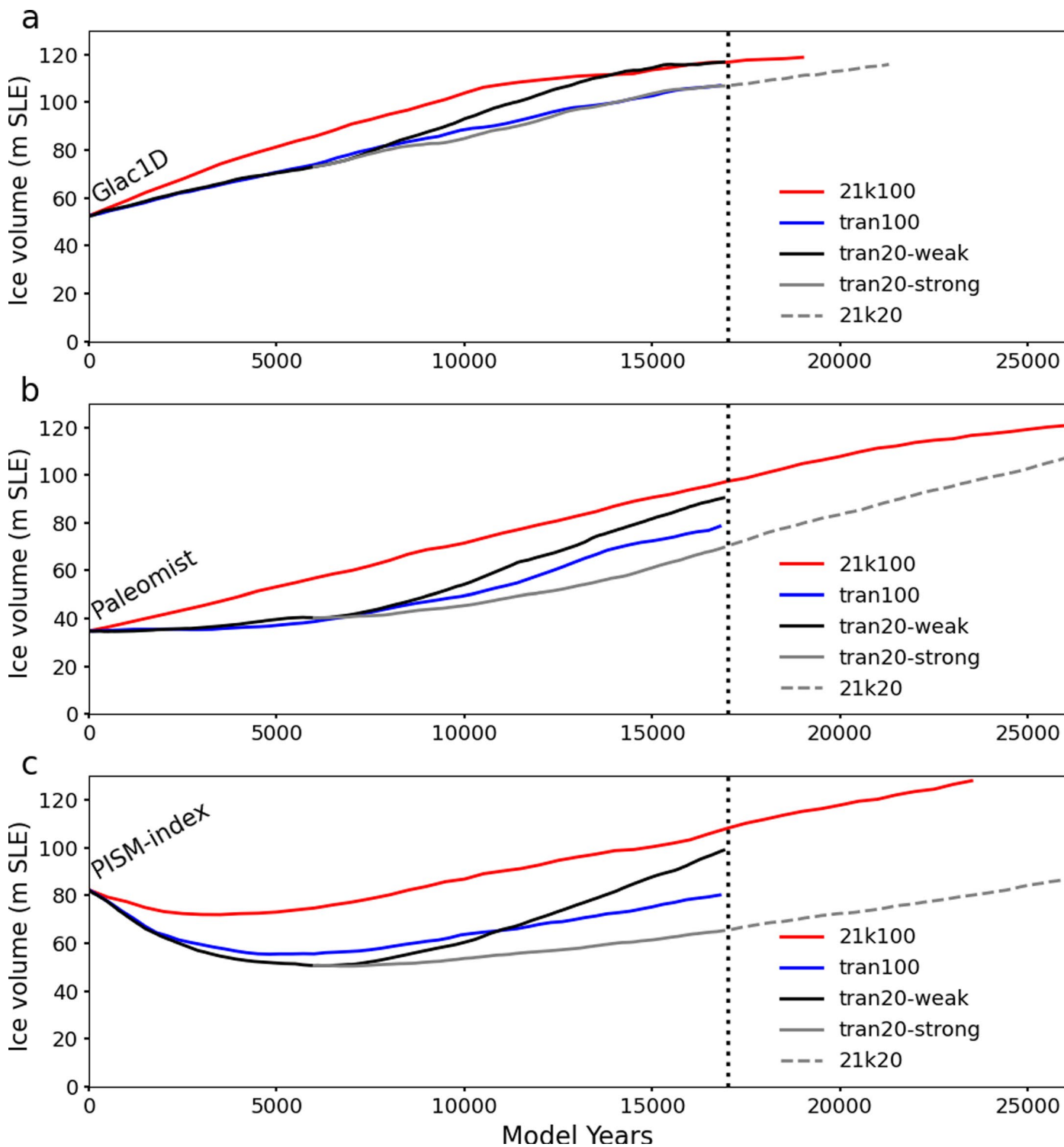
Extended Data Fig. 4 | Winter surface mass balance and snowfall changes of the North American ice sheets at different longitudes over time. Ice sheet margins at 38 ka, 28 ka and 21 ka from experiments **a)** Tran_Glac1d, **b)** Tran_Paleomist, **c)** Tran_PISMindex. Hovmöller Diagram of meridional mean winter (DJF) surface mass balance (SMB) of the North American ice sheets (NAIS) through different model years for experiments **d)** Tran_Glac1d, **e)**

Tran_Paleomist, **f)** Tran_PISMindex. **g-i)** same as **d-f**, but for snowfall. Black/grey contours in **d-i** represent latitudes of the southern margin of the NAIS at different longitudes. Contours that are dense along time axis indicate fast south expansion of the NAIS; contours that are dense along longitudes indicate longitudinally asymmetric distribution of the Laurentide Ice Sheet. The time axis corresponds to ice sheet model years.



Extended Data Fig. 6 | Climate changes between stadial and interstadial conditions (weak and strong AMOC) with orbital and Greenhouse gases forcing at 29 k. a) Surface temperature differences between simulated strong

and weak AMOC phases. **b)** same as **a**, but for precipitation. The dots represent the corresponding changes in paleoclimate proxy records, as show in Extended Data Tables 2–3 from Zhang et al.³⁰.



Extended Data Fig. 7 | Simulated ice volume changes of the North American ice sheets from various sensitivity experiments using different acceleration factors. Fixed 21 ka orbital and Greenhouse gases (GHGs) experiment with acceleration factor of 100 with different initial ice sheet conditions (red). Transient orbital and GHGs experiment with acceleration factor of 100 (blue). Transient

orbital and GHGs experiment with acceleration factor of 20 at weak (black) and strong (grey) AMOC conditions (dashed grey line represents continued experiment with fixed 21 ka orbital and GHGs). The experiments are initialized from different ice sheet boundary conditions: **a)** Glac1D-38k, **b)** Paleomist-38k, **c)** PISM-index-38k. Time axis corresponds to ice sheet model years.